ACS Catalysis

Research Article

pubs.acs.org/acscatalysis

Exploration of High-Performance Single-Atom Catalysts on Support M_1/FeO_x for CO Oxidation via Computational Study

Fengyu Li,[†] Yafei Li,[†] Xiao Cheng Zeng,*[,‡] and Zhongfang Chen*[,†]

[†]Department of Chemistry, University of Puerto Rico, Rio Piedras Campus, San Juan, Puerto Rico 00931, United States

[‡]Department of Chemistry, University of Nebraska—Lincoln, Lincoln, Nebraska 68588, United States

Supporting Information

ABSTRACT: Inspired by the recently discovered highly active CO oxidation catalyst Pt_1/FeO_x [Qiao, B.; Wang, A.; Yang, X.; Allard, L. F.; Jiang, Z.; Cui, Y.; Liu, J.; Li, J.; Zhang, T. *Nat. Chem.* **2011**, *3*, 634−641], we systemically examined various single-atom catalysts M_1/FeO_x (M = Au, Rh, Pd, Co, Cu, Ru and Ti) by means of density functional theory (DFT) computations, aiming at developing even more efficient and low-cost nanocatalysts for CO oxidation. Our computations identified five single-atom catalysts, namely the oxygen-defective Rh_1/FeO_x and Pd_1/FeO_x, Ru_1/FeO_x with or without oxygen vacancy, and vacancy-free Ti_1/FeO_x and Co_1/FeO_x, which exhibit improved overall catalytic performance compared to Pt_1/FeO_x for the CO oxidation via a Langmuir−Hinshelwood (LH) mechanism. These theoretical results provide new guidelines to design even more active and/or cost-effective heterogeneous catalysts for CO oxidation.

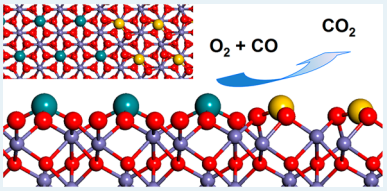

KEYWORDS: *single-atom catalyst, nonprecious metal, CO oxidation, density functional theory, Langmuir−Hinshelwood mechanism*

1. INTRODUCTION

Low-temperature CO oxidation is of both fundamental and practical importance in catalytic chemistry due to the impending demand of environmental protection (lowing emissions from automobiles and air purification in buildings) and the removal of CO contaminations from H_2-rich fuel gases for polymer electrolyte fuel cells (PEFC)[1] among many other industrial processes.

Supported metal clusters, especially those made of noble metals, e.g., Pt, Pd, Au, Rh, and Ru, are well-known catalysts for the CO oxidation. In their pioneering work, Haruta et al. revealed that Au clusters (less than 10 nm), when highly dispersed on transition metal oxides, can exhibit exceptional catalytic activity for low-temperature CO oxidation.[2] This exciting discovery has inspired extensive studies of the supported-metal catalysts for CO oxidation. However, the catalytic activities of supported metal nanoparticles can be strongly size- and shape-dependent;[2−5] moreover, the overall efficiency has been rather low on a per metal atom basis since only the surface atoms are active for catalysis. To address these scientific issues, single-atom catalysts have received increasing attentions owing to their intrinsic high activity, efficiency, and stability.[6] Indeed, heterogeneous catalysts with single-metal-atom dispersions are highly desired.[7−9]

From the experimental side, significant progresses have been made on the synthesis and characterization of single-metal atoms on various substrates, such as graphene,[10,11] zeolites, and open metal-oxide supports.[12−20] From the theoretical side, the catalytic activities of single-metal atom embedded on the graphene[21−25] or graphene oxide[26] or BN nanosheet[27−29] or iron oxide[30] have been studied. All previous studies demonstrated that uniformly dispersed single-metal atoms can serve as active sites for high performance catalysis.

Metal oxides are popular supports for heterogeneous catalysts. However, the stability and catalytic performance of single-metal atoms on metal oxides have been rarely studied. Recently, Qiao et al.[16] successfully anchored single Pt atoms to the iron-oxide surface, and they showed that such composite exhibits excellent stability and high activity for CO oxidation. They also elucidated the underlying reaction mechanism using density functional theory (DFT) computations. In another study, Ghosh and Nair investigated the O_2 activation and CO oxidation on Rh supported on γ-Al_2O_3 surface by ab initio molecular dynamics simulations, and they found the single-atom catalyst Rh_1/Al_2O_3 exhibits a much higher performance for CO oxidation than the Rh-cluster-based catalyst Rh_6/Al_2O_3.[31] The combination of enhanced activity/selectivity with reduced cost suggests that stable single-atom-based composites are promising to be a major form of heterogeneous catalysts for future applications.

Inspired by the exciting experimental discoveries and theoretical predictions, we systemically examined the catalytic activities of various single-metal atoms (Rh, Pd, Au, Co, Cu, Ru, and Ti) supported by the iron-oxide surface, using DFT computations. Our main goal is to find more efficient but less expensive catalysts for low-temperature CO oxidation than the highly active Pt_1/FeO_x[16] and to gain deeper insight into the associated reaction mechanisms. Our computations show that single Rh, Pd, Ru, and Ti atoms on iron-oxide surface exhibit superior catalytic performance for CO oxidation than Pt_1/FeO_x under the Langmuir−Hinshelwood (LH) mechanism. These single-atom nanocomposites offer new opportunities to develop more cost-effective heterogeneous catalysts with higher performance for CO oxidation.

Received: November 11, 2014
Published: December 8, 2014

DOI: 10.1021/cs501790v
ACS Catal. 2015, 5, 544−552

2. MODELS AND COMPUTATIONAL METHODS

The iron-oxide surface was modeled by an oxygen-terminated $Fe_2O_3(001)$ slab (FeO_x), the same as that used by Qiao et al.[16] This 1 × 1 supercell model includes 12 layers of Fe and 7 layers of O atoms (Figure S1), and the top 10 layers were fully relaxed in the computations. As used by Qiao et al.,[16] we also set the magnetic configuration as (+ − − +) for α-Fe_2O_3 slab with and without oxygen vacancy since this magnetic configuration is energetically the most favorable according to both previous prediction[32] and our test calculations. Our test calculations showed that further increase of the supercell size to 2 × 2 has little influence on the results of O_2/CO adsorption and reaction barriers of CO oxidation on Pt_1/FeO_x. Thus, the 1 × 1 supercell was used throughout the computations, and a 15 Å-width vacuum was added in the direction normal to the surfaces.

Our spin-polarized DFT computations were based on the generalized gradient approximation in the form of the Perdew−Burke−Ernzerhof exchange-correlation functional (PBE).[33] The frozen-core all-electron projector augmented wave (PAW) method[34] was used as implemented in the Vienna ab initio simulation package (VASP) code.[35] The Monkhorst−Pack scheme[36] of (3 × 3 × 1) k-points mesh was applied to carry out the numerical integrations in the reciprocal space. The kinetic energy cutoff for the plane-wave basis set was chosen to be 400 eV. Considering the strong electron correlation effects in metal-oxide supports, the calculations were carried out with the DFT+U method, and U = 4 eV for Fe was chosen based on previous studies.[16,37] However, U values were not added for the anchored single-metal atoms,[16] according to our test calculations on Rh_1/FeO_x, the PBE+U (U = 3.5 eV[38]) and PBE give quite close energy barriers of CO oxidation on Rh_1/FeO_x (0.43 eV of the first CO_2 formation for both cases). The computations on the isolated molecules and atoms were carried out in a (10 Å × 10 Å × 10 Å) unit cell with the Γ-point only for the k-point sampling. The reaction pathways were investigated by using the climbing-image nudged elastic band method (CI-NEB).[39] Transition states were characterized by vibrational frequency analysis with a single mode of imaginary frequency.

The formation energy (E_F) of an oxygen vacancy (O_{vac}) was evaluated by the following formula: $E_F = E_{Ovac} + 1/2E_{O2} - E_{pristine}$, where E_{Ovac}, E_{O2}, and $E_{pristine}$ are the total energies of the slab with an O_{vac}, the isolated oxygen molecule and the pristine slab, respectively. According to this definition, perfect slabs with smaller E_F values are more likely to form an O_{vac}.

The binding energy (E_b) of a metal atom or the adsorption energy (E_{ad}) of an adsorbate (O, O_2, CO, etc.) was defined as $E_b/E_{ad} = E + E' - E_{tot}$, where E, E', and E_{tot} represent the total energies of the clean slab, the isolated adsorbed atom/molecule, and the slab after adsorption, respectively. In the case of the coadsorption of two species A and B, E' is the sum of the total energies of isolated A and B. According to this definition, a positive (negative) value of E_b/E_{ad} indicates that the adsorption is exothermic (endothermic).

3. RESULTS AND DISCUSSION

3.1. Geometries and Stabilities of M_1/FeO_x (M = Au, Rh, Pd, Co, Cu, Ru, and Ti). We first considered all the possible anchored sites for single-metal atom M (M = Au, Rh, Pd, Co, Cu, Ru, and Ti) on iron-oxide surface without oxygen vacancies, namely, vacancy-free surface (Figure S1 and Table S1). Similar to Qiao et al.'s result,[16] the most stable sites for all the examined single metal atoms are the 3-fold hollow sites (Figure 1a). There

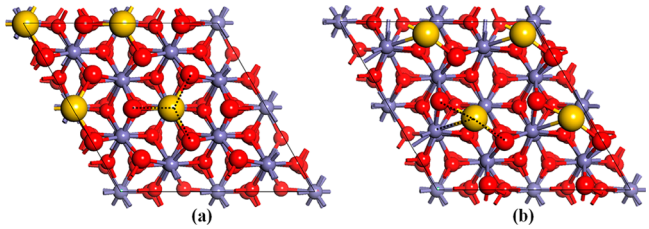

Figure 1. Top views of single metal atom M anchored on vacancy-free (a) and oxygen-defective (b) iron-oxide surfaces (M = Au, Rh, Pd, Co, Cu, and Ru). The dashed lines denote the bonds between M and the surface atoms. Color scheme: M, gold; O, red; Fe, purple.

are significant charge transfers from the single-metal atoms to iron-oxide surface (Hirshfeld charges[40] 0.35−0.68 |e|; see Table 1. The calculated q value for Pt is +0.45 |e| by Bader charge analysis[41] in Qiao et al.'s study.[16]). Among the examined single-metal atoms, Ti is closest to the bonded oxygen (d_{Ti-O} = 1.78 Å) and has the largest binding energy (13.03 eV) and the most positive charges (+0.68 |e|); while Au keeps the farthest to the surface oxygen (d_{Au-O} = 2.14 Å) and possesses the smallest E_b value (3.47 eV); Co is the least positively charged (+0.35 |e|).

We then examined the diffusion behavior of the anchored single metal atom (M = Au, Rh, Pd, Co, Cu, Ru, and Ti) on the iron-oxide FeO_x surface. The rather high diffusion barriers (E_d, 2.51−6.48 eV; see Table S2) of the individual metal atoms from the most stable site TH_c to the nearest Bridge_c or TH_d site (Figure S1) are comparable to or higher than the calculated E_d value (4.83 eV) of Pt from TH_c site to Bridge_c location, which exclude the aggregation of single metal atoms on the iron-oxide surface.

Next we studied the single metal atoms anchored on iron-oxide surface with oxygen vacancies (oxygen-defective surface), and in our model, each supercell contains one oxygen vacancy. Note that oxygen vacancies are inevitable, and generally oxygen vacancies on the support provide adsorption sites for the adsorbates and thus can facilitate CO oxidation[16,42,43] and other reactions.[44]

Compared to the formation of an oxygen vacancy on the pristine iron-oxide surface (~2.99 eV),[16] the presence of all the examined individual metal atoms facilitates the formation of oxygen vacancy on the iron-oxide surface, since the E_F values (0.69−2.85 eV, see Table 1) are all smaller than that of the clean iron-oxide surface. Among the examined metal atoms, Au-anchored iron-oxide surface has the lowest E_F value (0.69 eV). Compared to that on the pristine surface, on the oxygen-defective iron-oxide surface (Figure 1b), the binding strengths of the single metal atoms to the less coordinated oxygen are weakened by 0.72−2.97 eV and the electron transfers from metal atoms to the surface are reduced by 0.08−0.25 |e|. The binding energy between Ti and oxygen-defective FeO_x (10.06 eV) is still much stronger than those of other metal atoms, however, different from other protruding metals on oxygen-defective FeO_x surface, Ti is embedded into the oxygen defective site (see Figure S2).

Considering the unique energetically preferred configuration of Ti on oxygen-defective FeO_x (embedment into the defect site), and the O_2 dissociative adsorption on oxygen-defective Ru_1/FeO_x (see Section 3.2), below we will first discuss the O_2/CO adsorption and CO oxidation on oxygen-defective M_1/FeO_x (M = Au, Rh, Pd, Co, Cu, and Ru) and vacancy-free M_1/FeO_x (M = Au, Rh, Pd, Co, Cu, Ru, and Ti) surfaces.

DOI: 10.1021/cs501790v
ACS Catal. 2015, 5, 544−552

Table 1. Binding Energies (E_b, eV) of Single Metal Atom (Pt, Au, Rh, Pd, Co, Cu, Ru, and Ti) at the Most Stable Site (TH_c) of the Oxygen-Terminated Fe_2O_3 (001) Surface without Oxygen Vacancy, the Corresponding Hirshfeld Charges (q, $|e|$), the Formation Energies (E_F, eV) of an Oxygen Vacancy, and the Average Distance between the Single Metal Atom M and its Bonded Surface O/Fe ($d_{M\text{-}O}$ and d_{M-Fe}, Å)[a]

	Pt[b]	Au	Rh	Pd	Co	Cu	Ru	Ti
E_b	6.67	3.47	7.34	5.62	8.03	5.68	9.72	13.03
		2.75	5.26	4.27	6.12	4.25	6.83	10.06
q		+0.47	+0.48	+0.61	+0.35	+0.46	+0.53	+0.68
	+0.33	*+0.35*	*+0.40*	*+0.48*	*+0.27*	*+0.38*	*+0.40*	*+0.43*
d_{M-O}		2.14	1.89	2.01	1.82	1.84	1.83	1.78
	1.93	2.03	1.89	1.97	1.76	1.81	1.85	
d_{M-Fe}	2.52	2.61	2.55	2.62	2.51	2.61	2.52	
E_F	1.06	0.69	2.04	1.31	1.86	1.38	2.85	1.98

[a]The data in italics denote the corresponding parameters of single metal atom on oxygen-defective iron-oxide surface. [b]From ref 16.

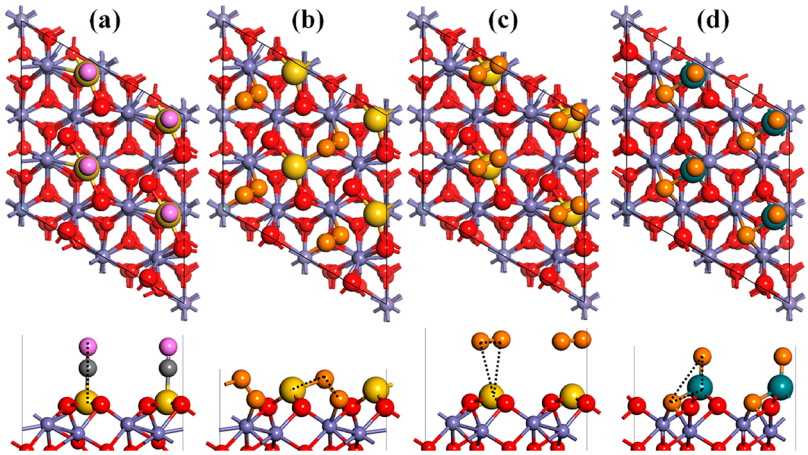

Figure 2. Top (upper) and side (lower) views of the energetically most favorable configurations of CO adsorbed on oxygen-defective M_1/FeO_x (M = Au, Rh, Pd, Co, Cu, and Ru) (a), O_2 adsorbed on oxygen-defective M_1/FeO_x (M = Rh, Pd, Co and Cu) (b), Au_1/FeO_x (c), and Ru_1/FeO_x (d). Color scheme: M, gold; Ru, cyan; C, gray; O of CO, pink; O of O_2, orange; O of the iron-oxide support, red; Fe, purple.

Table 2. Adsorption Energies (E_{ad}, eV) of CO and O_2 on Oxygen-Defective M_1/FeO_x (M = Pt, Au, Rh, Pd, Co, Cu, and Ru) and the Corresponding Key Geometry Parameters[a]

	Pt[b]	Au	Rh	Pd	Co	Cu	Ru	Ti
				CO				
E_{ad}	1.96	1.31	1.96	1.16	1.43	0.89	1.77	
	(1.08)	(1.49)	(0.97)	(0.80)	(1.61)	(0.65)	(1.54)	(0.90)
d_{C-O}		1.15	1.16	1.16	1.12	1.15	1.16	
		(1.15)	(1.16)	(1.15)	(1.15)	(1.15)	(1.17)	(1.15)
d_{M-C}		1.87	1.87	1.90	1.76	1.80	1.89	
		(1.88)	(1.80)	(1.91)	(1.91)	(1.89)	(1.82)	(2.21)
				O_2				
E_{ad}	1.05	−0.29	1.82	0.96	1.65	0.72	4.48	
	0.04	−0.04	1.14	0.96	0.94	*−0.37*	1.24	
		(0.14)	(0.79)	(0.48)	(0.54)	(−0.16)	(0.93)	(2.16)
d_{O-O}	1.46	1.36	1.44	1.39	1.43	1.34	3.19	
		(1.30)	(1.32)	(1.30)	(1.33)	(1.28)	(1.42)	(1.34)
d_{M-O}		2.03	1.91	1.95	1.73	1.86	1.69	
		(2.18)	(2.06)	(2.08)	(1.88)	(2.12)	(1.95)	(2.02)

[a]The C−O bond length d_{C-O}, the distance between metal atom M and the adjacent adsorbed O atom $d_{M\text{-}C}$; the O−O bond length d_{O-O}, the distance between metal atom M and the adjacent adsorbed O atom $d_{M\text{-}O}$, Å. The data in italic denote the adsorption energies of O_2 with O_2 parallel to the substrate. The data in parentheses represent the corresponding values on vacancy-free surfaces. [b]From ref 16.

3.2. Adsorption of CO and O_2 on Oxygen-Defective M_1/FeO_x (M = Au, Rh, Pd, Co, Cu, and Ru) and Vacancy-Free M_1/FeO_x (M = Au, Rh, Pd, Co, Cu, Ru, and Ti). For a catalyst, the ability to efficiently capture the adsorbates around the active site is an important criterion for catalytic performance. Understanding the O_2 and CO adsorption on M_1/FeO_x surfaces is the primary step to elucidate the catalytic mechanism of CO oxidation. Thus, we examined all the possible adsorption

DOI: 10.1021/cs501790v
ACS Catal. 2015, 5, 544−552

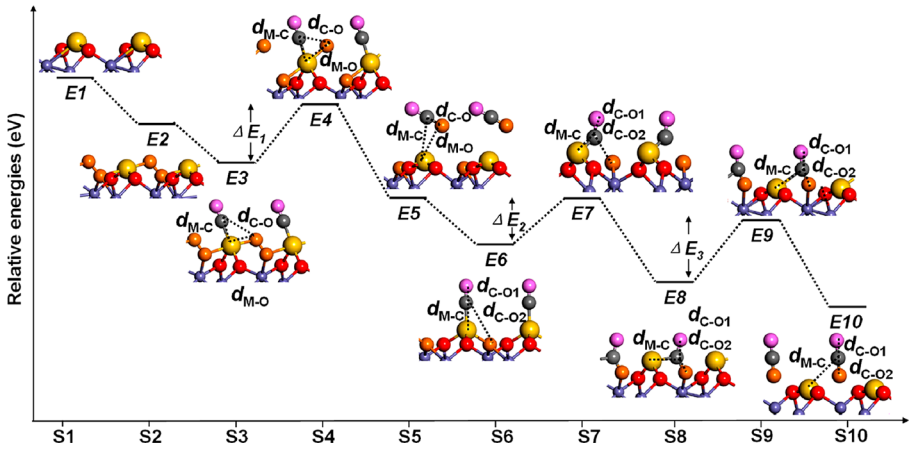

Figure 3. Reaction pathway of CO oxidation on oxygen-defective M_1/FeO_x (M = Pt, Rh, Pd, Co, and Cu) via the LH mechanism. Color scheme: M, gold; C, gray; O of O_2, orange; O of CO, pink; O of the iron-oxide support, red; Fe, purple.

configurations in order to search the energetically most favorable configuration for each adsorbate (O_2 and CO). The adsorption energies and key structural parameters of the lowest-energy configurations (see Figure 2) are summarized in Table 2.

For CO adsorption on all the examined M_1/FeO_x systems, regardless of the presence of the oxygen vacancy or not, the energetically most favorable configuration adopts an end-on structure (in which the O−C bond points to the metal atom perpendicularly or with only a small tilt angle to the FeO_x substrate, Figure 2a). The bond lengths of the adsorbed C−O (1.12−1.16 Å) deviate slightly from that of an isolated C−O molecule (1.14 Å). With the same CO adsorption energy of 1.96 eV, oxygen-defective Rh_1/FeO_x and Pt_1/FeO_x bind CO with the largest strength. The interaction between CO molecule and the other examined systems, M_1/FeO_x (M = Au, Pd, Co, Cu Ru, and Ti), are also significant (E_{ad} values are in between 0.65 and 1.77 eV).

For the O_2 adsorption on oxygen-defective M_1/FeO_x (M = Rh, Pd, Co, and Cu), the most favorable configuration (Figure 2b) is similar to the case of O_2 adsorption on Pt_1/FeO_x,[16] in which O_2 is elongated to 1.34−1.44 Å, one O atom of O_2 is adsorbed on the metal atom M, and the other O adsorbed to the O_{vac} periphery of the substrate. The binding energies are in the range of 0.72−1.82 eV.

However, O_2 does not prefer such a configuration on Au_1/FeO_x (E_{ad} = −0.29 eV). Even in the best configuration in which O_2 is parallel to the substrate (Figure 2c), the interaction is still weakly repulsive (E_{ad} = −0.04 eV). Thus, Au_1/FeO_x is very likely to be poisoned by CO, which is in line with the previous experimental findings that single Au atom on iron-oxide support is inactive for CO oxidation.[16,45] In this regard, the CO oxidation pathway will not be further studied on Au_1/FeO_x in the following section.

We tried to locate the configuration similar to Figure 2b by approaching O_2 molecule to oxygen-defective Ru_1/FeO_x with the tilt configuration of one O pointing to Ru and the other O close to the FeO_x surface O_{vac} region, surprisingly, O_2 dissociates spontaneously and leads to the lowest-energy configuration (Figure 2d) with a very high adsorption energy of 4.48 eV. We also located another configuration when attaching O_2 parallel to oxygen-defective Ru_1/FeO_x substrate (Figure 2c), the adsorbed O_2 is not dissociated, but the adsorption energy (1.24 eV) is much less than the best configuration and also weaker than that of CO molecule (1.77 eV).

For O_2 adsorption on vacancy-free M_1/FeO_x (M = Au, Rh, Pd, Co, Cu, and Ru), in the best configuration, O_2 is parallel to the substrate (similar to Figure 2c). Ti_1/FeO_x has the largest adsorption energy (2.16 eV), while Au_1/FeO_x (E_{ad} = 0.14 eV) and Cu_1/FeO_x (E_{ad} = −0.16 eV) has weak interaction even repulsion with O_2, and these two vacancy-free surfaces will not be further examined for CO oxidation.

Be aware of the recent report that CO induces Pd dispersion on $Fe_3O_4(001)$ surface,[46] we explored the possibility of CO-induced coalescence of Pd atoms supported on oxygen-defective $Fe_2O_3(001)$ surface. However, the unfavorable CO-induced Pd−O breakage (endothermic by 0.19 eV with a 1.11 eV energy barrier, see Figure S3) excludes the facile Pd mobility. Moreover, CO molecules also do not promote other considered metal adatoms clustering on the oxygen-defective FeO_x surface, for example, the Rh−O bond breaking with the existence of CO is endothermic by 1.60 eV, and the corresponding energy barrier is 2.81 eV. Considering that CO molecules do not induce M coalescence on oxygen-defective M_1/FeO_x, CO would not facilitate M aggregation on vacancy-free M_1/FeO_x in which M atom is bonded even stronger with the surface (with three M-O bonds vs two M-O bonds in the oxygen defective case).

3.3. Mechanism of CO Oxidation on M_1/FeO_x (M = Rh, Pd, Co, Cu, Ru, and Ti). Based on the different lowest-energy configurations of O_2 adsorbed on the different M_1/FeO_x as discussed above: molecular O_2 adsorption on oxygen-defective M_1/FeO_x (M = Rh, Pd, Co, and Cu), dissociated O_2 adsorption on oxygen-defective Ru_1/FeO_x, and molecular O_2 adsorption on vacancy-free M_1/FeO_x (M = Rh, Pd, Co, Ru, and Ti), we will discuss the mechanism of CO oxidation in three groups, namely, oxygen-defective M_1/FeO_x (M = Rh, Pd, Co, and Cu), oxygen-defective Ru_1/FeO_x, and vacancy-free M_1/FeO_x (M = Rh, Pd, Co, Ru, and Ti).

Oxygen-Defective M_1/FeO_x (M = Rh, Pd, Co, and Cu). Since O_2 and CO both are favorably adsorbed without dissociation on the M atom for these systems, we examined the LH mechanism for CO oxidation on M_1/FeO_x (M = Rh, Pd, Co, and Cu) as illustrated in Figure 3. The LH mechanism was also theoretically confirmed for CO oxidation on Pt_1/FeO_x[16] and proposed to rationalize the experimentally measured low activation energy of CO oxidation over Pt/FeO_x and Pd/FeO_x.[42] Note that on these oxygen-defective catalysts, the Eley−Rideal (ER) route is not preferred, since the ER starting state, i.e., CO approaching the adsorbed O_2 (O_2 adopts the energetically favorable configuration

DOI: 10.1021/cs501790v
ACS Catal. 2015, 5, 544−552

as shown in Figure 2d) is higher in energy (by 0.46−1.25 eV) than the CO and O_2 coadsorption state (**S3** in Figure 3).

The reaction starts from O_2 adsorption (**S2**) followed by the O_2/CO coadsorption on M_1/FeO_x (**S3**), where the adsorbed O_2 (O−O*) adopts the energetically most favorable configuration as in **S2** (one O adsorbed on the metal atom M and the other O adsorbed to the O_{vac} periphery of the substrate), while the adsorbed OC (OC*) adopts an end-on structure on the metal atom M, also similar to the case when a single CO molecule is adsorbed on M_1/FeO_x. Then, OC* approaches to O−O* to produce the first CO_2 (**S5**) by passing transition state **S4** in which the O−O* bond is further elongated, no intermediate is formed in this step. Afterward, the second CO molecule is adsorbed on M (**S6**) to form the intermediate OCO* (**S8**) by crossing the transition state **S7**; finally, passing the transition state **S9**, the second CO_2 is released from the surface (**S10**).

The above process can also be described as the successive reactions, OC* + O−O* → CO_2 + O* (step 1), CO* + O* → OCO* (step 2), and OCO* → CO_2 (step 3), and all of them follow the LH mechanism. The key geometry parameters and relative energies of each state were listed in Tables S3 and 3, respectively.

Table 3. Relative Energies (*E*1−*E*10, eV) of Each State (S1−S10) and Energy Barriers of Each Step in Figure 3 for Oxygen-Defective M_1/FeO_x (M = Pt,[16] Rh, Pd, Co, and Cu)

	Pt[a]	Rh	Pd	Co	Cu
*E*1	0.00	0.00	0.00	0.00	0.00
*E*2	−1.05	−1.82	−0.96	−1.65	−0.72
*E*3	−2.32	−3.06	−1.80	−2.95	−1.21
*E*4	−1.83	−2.63	−1.27	−2.19	−0.05
*E*5	−4.30	−4.56	−4.06	−6.32	−4.73
*E*6	−5.38	−5.54	−5.35	−7.90	−5.35
*E*7		−6.52	−4.78	−6.35	−4.73
*E*8	−6.29	−6.77	−5.70	−6.88	−6.12
*E*9	−5.50	−6.24	−5.15	−6.67	−6.30
*E*10	−6.49	−6.33	−5.53	−7.18	−6.44
ΔE_1	0.49	0.43	0.53	0.76	1.16
ΔE_2	0.00	0.00	0.57	1.55	0.62
ΔE_3	0.79	0.53	0.55	0.21	0.00

[a]From ref 16.

Among the four M_1/FeO_x surfaces examined above, both Rh_1/FeO_x and Pd_1/FeO_x have better overall performance for CO oxidation than Pt_1/FeO_x from both kinetic and thermodynamic aspects.

For the first CO_2 formation (step 1), Rh_1/FeO_x and Pd_1/FeO_x have lower or comparable energy barriers (0.43 and 0.53 eV) compared to Pt_1/FeO_x (0.49 eV),[16] while the barriers on Co_1/FeO_x (0.76 eV) and Cu_1/FeO_x (1.16 eV) are not so favorable. The reactions of step 1 on M_1/FeO_x are all exothermic by 2.30, 2.26, 3.37, and 3.52 eV for Rh, Pd, Co, and Cu, respectively.

In step 2, the second adsorbed CO molecule attacks the chemically adsorbed O atom to form the intermediate OCO* (**S8**). In this step, the formation of the intermediate on both Rh_1/FeO_x and Pd_1/FeO_x are exothermic (by 1.23 and 0.35 eV, respectively), especially this process is barrierless on Rh_1/FeO_x, the same as on Pt_1/FeO_x,[16] while that on Pd_1/FeO_x proceeds with a small barrier (0.57 eV). The OCO* formation on Cu_1/FeO_x is also exothermic (by 0.62 eV) with 0.77 eV activation barrier. However, in contrast to the high performance of Co_3O_4 nanomaterials,[47] on Co_1/FeO_x, this step is neither thermodynamically nor kinetically favored (endothermic by 1.02 eV with an activation barrier of 1.55 eV), which is similar to the case on Ir_1/FeO_x.[48]

In step 3, the second CO_2 is released from the surface. For this step, the energy barriers on Rh_1/FeO_x and Pd_1/FeO_x (0.53 and 0.55 eV, respectively) are lower than that on Pt_1/FeO_x (0.79 eV), and the CO_2 release is slightly endothermic (0.43 and 0.13 eV, respectively). Note that releasing CO_2 in this single step is more favorable on Co_1/FeO_x and Cu_1/FeO_x, it is barrierless on Cu_1/FeO_x, only a rather small barrier (0.21 eV) needs to be overcome on Co_1/FeO_x, and thermodynamically, it is exothermic on both surfaces (0.32 and 0.30 eV, respectively). The facile release of the second CO_2 indicates that in this step oxygen vacancies could be easily formed on Co_1/FeO_x and Cu_1/FeO_x; however, the rather high barriers in the first two steps limit their usages as effective catalysts for CO oxidation providing that the above pathways are followed in the reaction.

If we could reduce the high activation barrier in step 1 on Cu_1/FeO_x (1.16 eV), Cu_1/FeO_x could serve as a good catalyst for CO oxidation considering the other two favorable steps. Thus, we attempted to another pathway for step 1 following the CO self-promoting oxidation mechanism proposed and verified by Liu et al. very recently,[49] according to which the nearby adsorbed CO

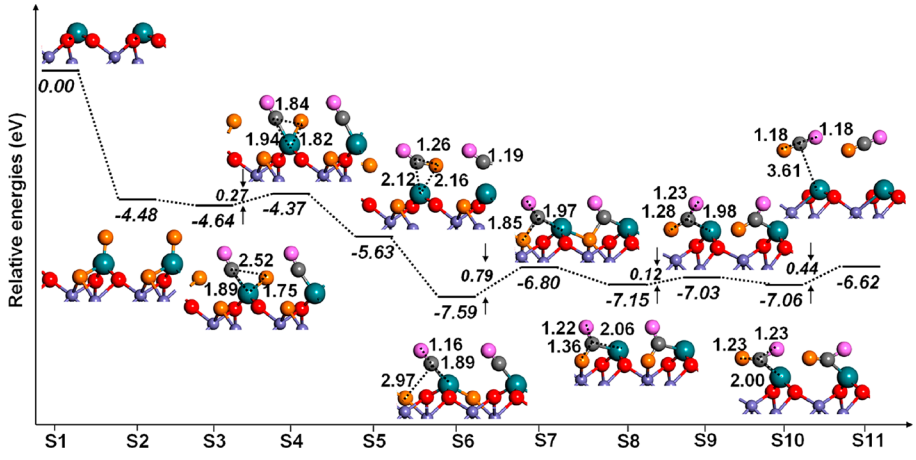

Figure 4. Reaction pathway of CO oxidation on oxygen-defective Ru_1/FeO_x via the LH mechanism. Color scheme: Ru, cyan; C, gray; O of O_2, orange; O of CO, pink; O of the iron-oxide support, red; Fe, purple.

DOI: 10.1021/cs501790v
ACS Catal. 2015, 5, 544−552

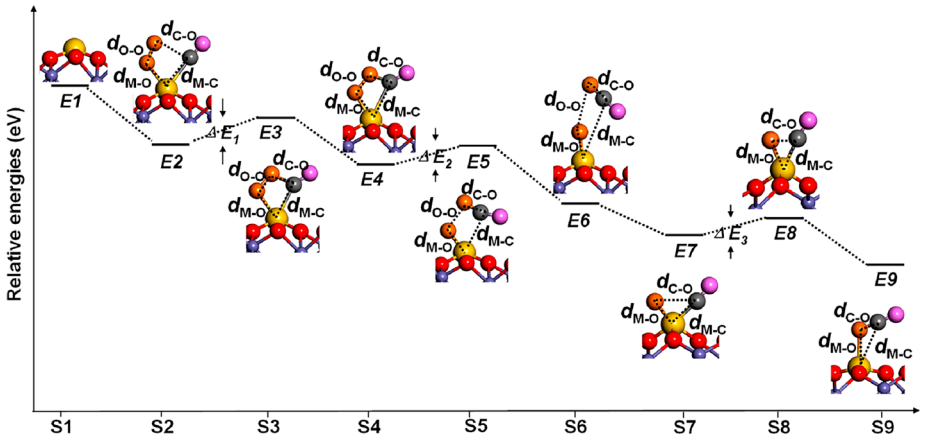

Figure 5. Reaction pathway of CO oxidation on vacancy-freee M_1/FeO_x (M = Ru, Rh, Pd, Co, and Ti) via the LH mechanism. Color scheme: M, gold; C, gray; O of O_2, orange; O of CO, pink; O of the iron-oxide support, red; Fe, purple.

molecule can promote the CO oxidation. Herein, Cu_1/FeO_x with a 2 × 1 × 1 supercell was adopted.

When two CO molecules are coadsorbed on O−O preadsorbed Cu_1/FeO_x (**S1** in Figure S4), the coadsorption energy per CO (0.81 eV) is nearly twice as a solo CO is coadsorbed with O−O in a unit cell (0.49 eV). Unexpectedly, the coadsorption of two CO molecules does not promote O_2 dissociation to form a CO_2 and an intermediate OCO* (**S4** in Figure S3), the energy barrier (1.40 eV) is even higher than those for O−O bond breakage (1.16 eV) and OCO* formation (0.62 eV) when a solo CO and O_2 are coadsorbed on Cu_1/FeO_x via the LH mechanism.

Oxygen-Defective Ru_1/FeO_x. Ru_1/FeO_x with oxygen vacancy has rather high activity for O_2 dissociation (**S2**, Figure 5), after the first CO is adsorbed (**S3**), the availability of the activated O atom leads to a rather low energy barrier (0.27 eV for **S4**) and favorable exothermity (1.26 eV) for the first CO_2 formation (**S5**) via the LH mechanism (Figure 4). Concomitantly with the removal of O atom on Ru, the remained surface recovers to the vacancy-free surface. Afterward, the CO migrates in the reaction complex formed by the second CO adsorption (**S6**) to form OCO* intermediate (**S8**) by crossing a 0.79 eV barrier (**S7**). Then, passing a very low energy barrier of 0.12 eV (**S9**), the breakage of O−Fe bond between OCO and Fe atom leads to **S10** with CO_2 single-bonded to Ru atom on the Ru_1/FeO_x surface.

We also considered the ER mechanism for the first CO oxidation with the atomic O on Ru. However, compared to the LH mechanism, such a step requires a slightly higher energy barrier (0.47 eV) with less exothermality (0.65 eV) (see Figure S5).

In all the above the LH mechanism on oxygen-defective M_1/FeO_x (M = Rh, Pd, Co, Cu, and Ru) surfaces, following the preferred LH mechanism, after the first CO_2 formation, the remaining O fills the oxygen vacancy and restores the vacancy-free surface. The oxygen vacancy can be regenerated if the second CO_2 formation is thermodynamically favorable as in Pt_1/FeO_x.[16] However, the second CO_2 formation on oxygen-defective Co_1/FeO_x and Ru_1/FeO_x is endothermic, implying that the regeneration of oxygen vacancy on these two surfaces is not preferred, which is in line with their higher formation energies of an oxygen vacancy (E_F = 1.86 and 2.85 eV, respectively) than that of Pt_1/FeO_x (1.06 eV).[16] Moreover, the E_F values of Rh_1/FeO_x, Pd_1/FeO_x and Ti_1/FeO_x (2.04, 1.31, and 1.98 eV, respectively) are also higher than that of Pt_1/FeO_x.[16] Thus, we also studied the performance of CO oxidation over Rh, Pd, Co, Ru and Ti anchored on iron-oxide surface without oxygen vacancies.

Vacancy-Free M_1/FeO_x (M = Ru, Rh, Pd, Co, and Ti). For vacancy-free M_1/FeO_x (M = Ru, Rh, Pd, Co, and Ti) surfaces, we examined both LH and ER mechanisms.

In the LH mechanism as shown in Figure 5, O_2 and CO are coadsorbed first (**S2**), then cross a barrier of ΔE_1 to form the intermediate OOCO* on M (**S4**) and subsequently the first CO_2 (**S6**) is released by surpassing ΔE_2 energy barrier; finally, the second CO_2 production (**S7** → **S8** → **S9**) has to overcome a barrier of ΔE_3. The LH process can also be described as the successive reactions, OC* + OO* → OOCO* (step 1), OOCO* → O* + CO_2 (step 2), and O* + CO* → CO_2 (step 3). The key geometry parameters and relative energies of each state were listed in Tables S4 and 4, respectively.

Table 4. Relative Energies (*E*1−*E*9, eV) of Each State (S1−S9) and Energy Barriers of Each Step in Figure 5 for Vacancy-Free M_1/FeO_x (M = Ru, Rh, Pd, Co, and Ti)

	Ru	Rh	Pd	Co	Ti
*E*1	0.00	0.00	0.00	0.00	0.00
*E*2	−1.82	−1.59	−1.17	−1.05	−1.53
*E*3	−1.56	−0.94	−0.34	−0.60	−1.16
*E*4	−2.08	−1.65	−1.03	−1.57	−1.64
*E*5		−0.98			
*E*6	−5.57	−4.30		−4.11	−4.04
*E*7	−5.73	−3.36		−4.35	−4.61
*E*8	−5.46	−3.25			
*E*9	−6.72	−5.08		−6.71	−6.85
ΔE_1	0.26	0.65	0.83	0.45	0.37
ΔE_2	0.00	0.67		0.00	0.00
ΔE_3	0.27	0.11		0.00	0.00

For the intermediate OOCO* formation (step 1), Ru_1/FeO_x, Co_1/FeO_x, and Ti_1/FeO_x have very low energy barriers (0.26, 0.37, and 0.45 eV, respectively), and the barriers on Rh_1/FeO_x (0.65 eV) is also satisfactory. However, the relatively high barrier on Pd_1/FeO_x (0.83 eV) for the step 1 disqualifies this surface as an optimal catalyst, thus further reaction steps on this surface were not examined. In step 2, the release of the first CO_2 molecule is spontaneous without any barrier on Ru_1/FeO_x, Co_1/FeO_x, and Ti_1/FeO_x, while on Rh_1/FeO_x it has to pass through state **S5** by overcoming a barrier of 0.67 eV; In step 3, the remained atomic oxygen on M is removed by the second CO_2

DOI: 10.1021/cs501790v
ACS Catal. 2015, 5, 544−552

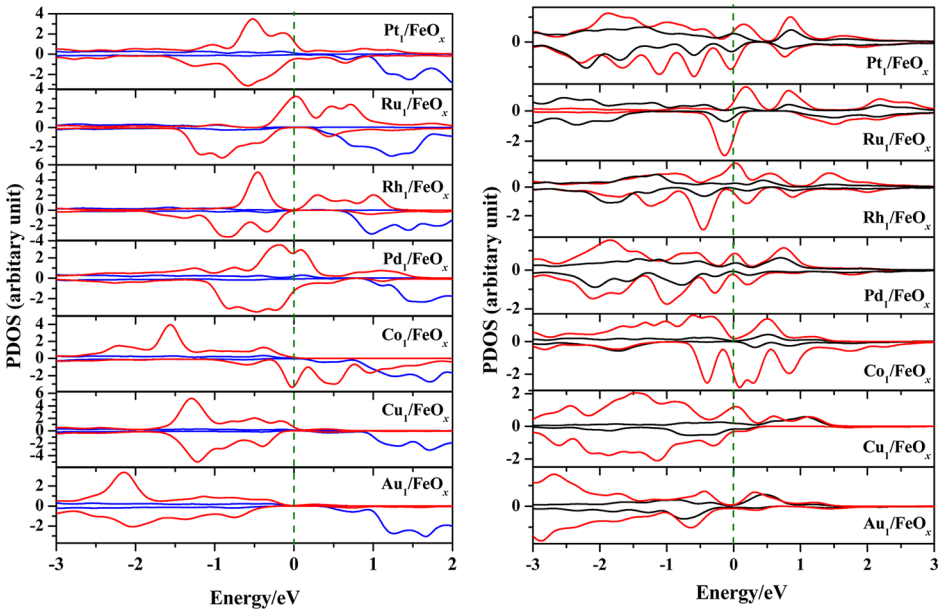

Figure 6. Calculated PDOS for top layer M-*d* orbital (red) and subtop layer Fe-*d* orbital (blue) and of oxygen-defective M_1/FeO_x, M = Pt, Ru, Rh, Pd, Co, Cu, and Au (left panel), and their corresponding PDOS (right panel) for M-*d* orbital (red) and adsorbed O_2-*p* orbital (black). The Fermi energy was set zero indicated by the vertical dashed line.

formation, the energy barriers on Co_1/FeO_x and Ti_1/FeO_x are negligible, and those on Ru_1/FeO_x and Rh_1/FeO_x are only 0.27 and 0.11 eV, respectively. However, the adsorption of the CO to the atomic O on Rh is endothermic by 0.94 eV, indicating the unfavorable process of removing the atomic O on Rh_1/FeO_x surface.

For the ER mechanism, in which the CO molecules directly react with the activated O_2. Among the five examined vacancy-free M_1/FeO_x (M = Ru, Rh, Pd, Co, and Ti) catalysts, the adsorbed O_2 molecule on Ru_1/FeO_x is best activated (O−O bond length 1.42 Å). Our computations showed that even on Ru_1/FeO_x the ER reaction mechanism is not kinetically favorable (see Figure S6 and S7), which excludes the preference of ER pathways for the catalysts examined here.

Among the five vacancy-free M_1/FeO_x surfaces examined above, Ru_1/FeO_x is highly active for CO oxidation, Co_1/FeO_x has better performance for CO oxidation than its oxygen-defective counterpart from both kinetic and thermodynamic aspects, Ti_1/FeO_x also exhibits superior accomplishment, while the catalytic capability for CO oxidation on vacancy-free Rh_1/FeO_x and Pd_1/FeO_x is lower than on their oxygen-defective counterparts.

3.4. Understanding of the Catalytic Performance. In the proceeding sections, we have discussed the CO oxidation over two groups of single-atom catalysts, namely oxygen-defective M_1/FeO_x (M = Rh, Pd, Co, and Cu) and vacancy-free M_1/FeO_x (M = Ru, Rh, Pd, Co, and Ti). The following conclusion can be obtained: (1) among oxygen defective M_1/FeO_x (M = Pt,[16] Rh, Pd, Co, and Cu) with similar LH CO oxidation pathways, Rh_1/FeO_x distinguishes itself by having the low energy barrier at each reaction step, the performance of Pd_1/FeO_x is also appreciable; on Co_1/FeO_x and Cu_1/FeO_x, the second CO_2 formation is rather facile but the formation of the first CO_2 is kinetically unfavored; (2) the oxygen-defective Ru_1/FeO_x exhibits very high activity toward O_2 dissociation, however, the oxygen vacancy on Ru_1/FeO_x can be easily recovered to vacancy-free surface by O_2 dissociation and the facile removal of the dissociated O adsorbed on Ru. Luckily, the vacancy-free Ru_1/FeO_x also performs well for CO oxidation. Thus, regardless the oxygen vacancy is available or not, Ru_1/FeO_x possesses remarkable performance on the CO oxidation via L-H mechanism with very low activation energies; (3) vacancy-free Co_1/FeO_x and Ti_1/FeO_x exhibit comparable performance and similar reaction routes with vacancy-free Ru_1/FeO_x. All the activation energies on vacancy-free Co_1/FeO_x and Ti_1/FeO_x are smaller than 0.45 eV via the LH mechanism. Overall, the performances of oxygen-defective Rh_1/FeO_x and Pd_1/FeO_x, vacancy-free Ru_1/FeO_x, Ti_1/FeO_x, and Co_1/FeO_x are all better than Pt_1/FeO_x,[16] the highly active low-temperature CO oxidation catalyst reported very recently.

To understand the different catalytic behavior of M_1/FeO_x (M = Pt,[16] Rh, Ru, Pd, Co, Cu, and Ti) toward CO oxidation, we explored the electronic structures of these heterogeneous catalysts. Comparing the projected density of states (PDOS) for the M atom and its most adjacent O and Fe atoms of the oxygen-defective M_1/FeO_x slabs (Figure 6, left panel), we found that the *d*-band center of M_1/FeO_x (M = Pt, Rh, Pd, and Ru) is significantly shifted to higher energy respect to the inactive Au_1/FeO_x, thereby these catalysts have more empty *d* states and hence stronger interaction with adsorbates (O_2 and CO), which is consistent with the high adsorption energies of adsorbates on these slabs and their high catalytic activity. Taking O_2 adsorption (**S2** in Figure 3) as an example (Figure 6, right panel), there are obvious hybridizations between the O_2-*p* orbitals and M-*d* orbitals (M = Pt, Rh, and Pd) in both spin-up and spin-down channels, thereby leading to the significantly activated O_2 on these surfaces to facilitate CO oxidation; in comparison, the hybridization between the O_2-*p* orbitals and M-*d* orbitals (M = Co, Cu, and Au) are much weaker. Similarly, the *d*-band center of vacancy-free M_1/FeO_x (M = Ru, Ti, and Co) slabs, which has remarkable CO oxidation performance, also shifts upward in energy with respect to oxygen-defective Pt_1/FeO_x surface (Figure S8). Moreover, for the O_2 and CO coadsorption state (**S2** in Figure 5), the CO antibonding states well hybridize with the M-*d* orbital on these three catalysts, which lead to facile formation of the intermediate OOCO*. In contrast, on vacancy-free Pd_1/FeO_x the hybridization is rather poor (Figure S8),

DOI: 10.1021/cs501790v
ACS Catal. 2015, 5, 544−552

resulting in a much higher activation barrier for OOCO* formation. In general, the catalysts with *d*-band center shifted to higher energies have enhanced catalytic performance.[50]

4. CONCLUSION

In the present work, we carried out a comprehensive study of the stability and CO oxidation activity of single-atom heterogeneous catalysts, M_1/FeO_x (M = Pd, Ru, Rh, Au, Co, Cu, and Ti), by means of DFT computations. The systems examined have very high stability (higher than or comparable to the recently synthesized Pt_1/FeO_x), as indicated by the strong binding energies and high diffusion barriers of the single-metal atoms on the FeO_x support. Among all the considered single-metal atom systems, Ru_1/FeO_x distinguishes itself on the CO oxidation by having very low activation energy in each step, regardless of the existence or absence of oxygen vacancy; vacancy-free Co_1/FeO_x and Ti_1/FeO_x exhibit comparable performance and similar reaction routes with vacancy-free Ru_1/FeO_x. The CO oxidation on the oxygen-defective M_1/FeO_x (M = Pt,[16] Rh, Co, and Cu) follows the similar mechanism, and among them Rh_1/FeO_x performs the best; Au_1/FeO_x is very likely to be poisoned by CO. All the reactions on these heterogeneous catalysts prefer the LH mechanism.

In summary, our extensive search gives rise to five single-atom catalysts, namely oxygen-defective Rh_1/FeO_x and Pd_1/FeO_x, Ru_1/FeO_x with or without oxygen vacancy, and vacancy-free Co_1/FeO_x and Ti_1/FeO_x surface, whose catalytic performance for CO oxidation approach to or exceed the highly active Pt_1/FeO_x.[16] Especially, Co_1/FeO_x and Ti_1/FeO_x with nonprecious metals possess very low activation energies for CO oxidation via the LH mechanism. These heterogeneous catalysts can be experimentally achieved using the similar approach as for Pt_1/FeO_x[16] and Ir_1/FeO_x.[48] This study may open a new avenue for designing advanced nanocatalysts with less usage of expensive metals, enhanced selectivity and activity for low-temperature CO oxidation. We wish experimental confirmation of the remarkable performance of single-atom catalysts for the CO oxidation can be done in near future.

■ ASSOCIATED CONTENT

Supporting Information

The following file is available free of charge on the ACS Publications website at DOI: 10.1021/cs501790v.

Binding energies of single metal atom (Pt, Pd, Ru, Rh, Au, Co, Cu, and Ti) at different anchored sites of oxygen terminated Fe_2O_3 (001) surface, the diffusion barriers of single metal atom from the energetically most preferred TH_c site to its adjacent site on oxygen terminated Fe_2O_3 (001) surface, the key geometric parameters of each state in Figure 3 (**S3**−**S10**) and in Figure 4 (**S2**−**S9**), illustration of different anchored sites for single metal atom on vacancy-free Fe_2O_3(001) surface, top and side views of single Ti atom embedded in oxygen-defective iron oxide surface, illustration of CO-induced Pd migration on FeO_x surface, reaction pathway of CO oxidation on oxygen-defective Cu_1/FeO_x via CO self-promoting mechanism, reaction pathway of CO oxidation on oxygen-defective and vacancy-free Ru_1/FeO_x via the ER mechanism, calculated PDOS for M-*d* orbital and the top layer Fe-*d* orbital of the vacancy-free M_1/FeO_x (M = Ru, Rh, Pd, Co, and Ti), and their corresponding PDOS for M-*d* orbital, coadsorbed CO-*p* and O_2-*p* orbital (PDF)

■ AUTHOR INFORMATION

Corresponding Authors

*E-mail: zhongfangchen@gmail.com (Z.C.).
*E-mail: xzeng1@unl.edu (X.C.Z).

Notes

The authors declare no competing financial interest.

■ ACKNOWLEDGMENTS

Support by National Science Foundation (Grant EPS-1010094) and University of Nebraska Holland Computing Center is gratefully acknowledged.

■ REFERENCES

(1) Liu, K.; Wang, A.; Zhang, T. *ACS Catal.* **2012**, *2*, 1165−1178.
(2) Haruta, M.; Yamada, N.; Kobayashi, T.; Iijima, S. *J. Catal.* **1989**, *115*, 301−309.
(3) Judai, K.; Abbet, S.; Wörz, A. S.; Heiz, U.; Henry, C. R. *J. Am. Chem. Soc.* **2004**, *126*, 2732−2737.
(4) Schalow, T.; Brandt, B.; Starr, D. E.; Laurin, M.; S. Shaikhutdinov, K.; Schauermann, S.; Libuda, J.; Freund, H.-J. *Angew. Chem., Int. Ed.* **2006**, *45*, 3693−3697.
(5) Rodriguez, J. A.; Liu, P.; Takahashi, Y.; Viñes, F.; Feria, L.; Florez, E.; Nakamura, K.; Illas, F. *Catal. Today* **2011**, *166*, 2−9.
(6) Yang, X.; Wang, A.; Qiao, B.; Li, J.; Liu, J.; Zhang, T. *Acc. Chem. Res.* **2013**, *46*, 1740−1748.
(7) Fu, Q.; Saltsburg, H.; Flytzani-Stephanopoulos, M. *Science* **2003**, *301*, 935−938.
(8) Kyriakou, G.; Boucher, M. B.; Jewell, A. D.; Lewis, E. A.; Lawton, T. J.; Baber, A. E.; Tierney, H. L.; Flytzani-Stephanopoulos, M.; Sykes, E. C. H. *Science* **2012**, *335*, 1209−1212.
(9) Fang, H.-C.; Li, Z. H.; Fan, K.-N. *Phys. Chem. Chem. Phys.* **2011**, *13*, 13358−13369.
(10) Sun, S.; Zhang, G.; Gauquelin, N.; Chen, N.; Zhou, J.; Yang, S.; Chen, W.; Meng, X.; Geng, D.; Banis, M. N.; Li, R.; Ye, S.; Knights, S.; Botton, G. A.; Sham, T.-K.; Sun, X. *Sci. Rep.* **2013**, *3*, 1775.
(11) Eelbo, T.; Waśniowska, M.; Thakur, P.; Gyamfi, M.; Sachs, B.; Wehling, T. O.; Forti, S.; Starke, U.; Tieg, C.; Lichtenstein, A. I.; Wiesendanger, R. *Phys. Rev. Lett.* **2013**, *110*, 136804.
(12) Abbet, S.; Heiz, U.; Hakkinen, H.; Landman, U. *Phys. Rev. Lett.* **2001**, *26*, 5950.
(13) Novoný, Z.; Argentero, G.; Wang, Z.; Schmid, M.; Diebold, U.; Parkinson, G. *Phys. Rev. Lett.* **2012**, *108*, 216103.
(14) Flytzani-Stephanopoulos, M.; Gates, B. C. *Annu. Rev. Chem. Biomol. Eng.* **2012**, *3*, 545−574.
(15) Huang, Z.; Gu, X.; Cao, Q.; Hu, P.; Hao, J.; Li, J.; Tang, X. *Angew. Chem., Int. Ed.* **2012**, *51*, 4198−4203.
(16) Qiao, B.; Wang, A.; Yang, X.; Allard, L. F.; Jiang, Z.; Cui, Y.; Liu, J.; Li, J.; Zhang, T. *Nat. Chem.* **2011**, *3*, 634−641.
(17) Moses-DeBusk, M.; Yoon, M.; Allard, L. F.; Mullins, D. R.; Wu, Z.; Yang, X.; Veith, G.; Stocks, G. M.; Narula, C. K. *J. Am. Chem. Soc.* **2013**, *135*, 12634−12645.
(18) Lin, J.; Wang, A.; Qiao, B.; Liu, X.; Yang, X.; Wang, X.; Liang, J.; Li, J.; Liu, J.; Zhang, T. *J. Am. Chem. Soc.* **2013**, *135*, 15314−15317.
(19) Xing, J.; Chen, J. F.; Li, Y. H.; Yuan, W. T.; Zhou, Y.; Zheng, L. R.; Wang, H. F.; Hu, P.; Wang, Y.; Zhao, H. J.; Wang, Y.; Yang, H. G. *Chem.—Eur. J.* **2014**, *20*, 2138−2144.
(20) Bruix, A.; Lykhach, Y.; Matolínová, I.; Neitzel, A.; Skála, T.; Tsud, N.; Vorokhta, M.; Stetsovych, V.; Ševčiková, K.; Myslivček, J.; Prince, K. C.; Bruyere, S.; Potin, V.; Illas, F.; Matolín, V.; Libuda, J.; Neyman, K. M. *Angew. Chem., Int. Ed.* **2014**, *53*, 10525−10530.
(21) Tang, Y.; Yang, Z.; Dai, X. *Phys. Chem. Chem. Phys.* **2012**, *14*, 16566−16572.
(22) Lu, Y. H.; Zhou, M.; Zhang, C.; Feng, Y. P. *J. Phys. Chem. C* **2009**, *113*, 20156−20160.
(23) Li, Y.; Zhou, Z.; Yu, G.; Chen, W.; Chen, Z. *J. Phys. Chem. C* **2010**, *114*, 6250−6254.

DOI: 10.1021/cs501790v
ACS Catal. 2015, 5, 544−552

(24) Song, E. H.; Wen, Z.; Jiang, Q. *J. Phys. Chem. C* **2011**, *115*, 3678−3683.
(25) Wannakao, S.; Nongnual, T.; Khongpracha, P.; Maihom, T.; Limtrakul, J. *J. Phys. Chem. C* **2012**, *116*, 16992−16998.
(26) Li, F.; Zhao, J.; Chen, Z. *J. Phys. Chem. C* **2012**, *116*, 2507−2514.
(27) Zhao, P.; Su, Y.; Zhang, Y.; Li, S. J.; Chen, G. *Chem. Phys. Lett.* **2011**, *515*, 159−162.
(28) Huang, C.; Ye, X.; Chen, C.; Lin, S.; Xie, D. *Comput. Theor. Chem.* **2013**, *1011*, 5−10.
(29) Lin, S.; Ye, X.; Johnson, R. S.; Guo, H. *J. Phys. Chem. C* **2013**, *117*, 17319−17326.
(30) Yu, X.; Wang, S.; Li, Y.; Wang, J.; Jiao, H. *J. Phys. Chem. C* **2012**, *116*, 10632−10638.
(31) Ghosh, T. K.; Nair, N. N. *ChemCatChem.* **2013**, *5*, 1811−1821.
(32) Sandratskii, L. M.; Uhl, M.; Kübler, J. *J. Phys.: Condens. Matter* **1996**, *8*, 983−989.
(33) Perdew, J. P.; Burke, K.; Ernzerhof, M. *Phys. Rev. Lett.* **1996**, *77*, 3865−3868.
(34) Blöchl, P. E. *Phys. Rev. B* **1994**, *50*, 17953−17979.
(35) Kresse, G.; Furthmüller, J. *Phys. Rev. B* **1996**, *54*, 11169−11186.
(36) Monkhorst, H. J.; Pack, J. D. *Phys. Rev. B* **1976**, *13*, 5188−5192.
(37) Rollmann, G.; Rohrbach, A.; Entel, P.; Hafner, J. *Phys. Rev. B* **2004**, *69*, 165107.
(38) Scherson, Y. D.; Aboud, S. J.; Wilcox, J.; Cantwell, B. J. *J. Phys. Chem. C* **2011**, *115*, 11036−11044.
(39) Henkelman, G.; Uberuaga, B. P.; Jónsson, H. *J. Chem. Phys.* **2000**, *113*, 9901−9904.
(40) Hirshfeld, F. L. *Theoret. Chim. Acta B* **1977**, *44*, 129−138.
(41) Henkelman, G.; Arnaldsson, A.; Jónsson, H. *Comput. Mater. Sci.* **2006**, *36*, 254−360.
(42) Liu, L.; Zhou, F.; Wang, L.; Qi, X.; Shi, F.; Deng, Y. *J. Catal.* **2010**, *274*, 1−10.
(43) Liu, L.; Cai, J.; Qia, L.; Yua, Q.; Sun, K.; Liu, B.; Gao, F.; Dong, L.; Chen, Y. *J. Mol. Catal. A: Chem.* **2010**, *327*, 1−11.
(44) Calaza, F. C.; Xu, Y.; Mullins, D. R.; Overbury, S. H. *J. Am. Chem. Soc.* **2012**, *134*, 18034−18045.
(45) Herzing, A. A.; Kiely, C. J.; Carley, A. F.; Landon, P.; Hutchings, G. J. *Science* **2008**, *321*, 1331−1335.
(46) Parkinson, G. S.; Novotny, Z.; Argentero, G.; Schmid, M.; Pavelec, J.; Kosak, R.; Blaha, P.; Diebold, U. *Nat. Mater.* **2013**, *12*, 724−728.
(47) (a) Tüysüz, H.; Comotti, M.; Schüth, F. *Chem. Commun.* **2008**, 4022−4024. (b) Xie, X.; Li, Y.; Zhi-Quan, L.; Haruta, M.; Shen, W. *Nature* **2009**, *458*, 756−749. (c) Jia, C. J.; Schwickardi, M.; Weidenthaler, C.; Schmidt, W.; Korhonen, S.; Weckhuysen, B. M.; Schüth, F. *J. Am. Chem. Soc.* **2011**, *133*, 11279−11288.
(48) Liang, J.; Lin, J.; Yang, X.; Wang, A.; Qiao, B.; Liu, J.; Zhang, T.; Li, J. *J. Phys. Chem. C* **2014**, *118*, 21945−21951.
(49) Liu, C.; Tan, Y.; Lin, S.; Li, H.; Wu, X.; Li, L.; Pei, Y.; Zeng, X. C. *J. Am. Chem. Soc.* **2013**, *135*, 2583−2595.
(50) Hamme, B.; Nørskov, J. K. Theoretical surface science and catalysis—calculations and concepts. *Impact of Surface Science on Catalysis*; Advances in Catalysis; Elsevier, 2000, Vol. *45*; pp 71−129.

DOI: 10.1021/cs501790v
ACS Catal. 2015, 5, 544−552